

Key role of oxidizing species driving water oxidation revealed by time-resolved optical and X-ray spectroscopies

Received: 1 July 2025

Accepted: 23 January 2026

Published online: 26 February 2026

Check for updates

Caiwu Liang^{1,2}✉, Lucas Garcia Verga¹, Benjamin Moss^{2,7}, Santosh Kumar³, Soren B. Scott⁴, Mark A. Turner⁵, Pilar Ferrer³, Veronica Celorrio³, Dave C. Grinter³, Yemin Tao¹, Sid Halder¹, Yifeng Wang¹, Cindy Tseng¹, Guangmeimei Yang², Georg Held³, Sarah J. Haigh⁵, Aron Walsh¹, Ifan E. L. Stephens¹✉, James R. Durrant^{2,6}✉ & Reshma R. Rao¹✉

Oxidation states underpin the understanding of active states, reaction mechanisms and catalytic performance of electrocatalysts. However, determining them at complex solid–liquid interfaces is challenging. Here we use multimodal spectroscopy to investigate polarized iridium oxide (IrO_x) electrodes, a model water oxidation catalyst, to identify potential-dependent iridium and oxygen oxidation states. By integrating multiple operando spectroscopies (optical (ultraviolet–visible), Ir L-edge and O K-edge X-ray absorption spectroscopy) with electrochemistry mass spectrometry and density functional theory calculations, we identify the sequential depletion of electron densities from the Ir5*d* band (corresponding to Ir³⁺→Ir⁴⁺→Ir⁵⁺), followed by electron removal from the O2*p* band, forming electrophilic oxygen species (O⁻¹) due to enhanced Ir–O covalency and electronic state overlap. Time-resolved measurements reveal distinct lifetimes for Ir⁵⁺ and O⁻¹ states under water oxidation conditions, Ir⁵⁺ remains unreactive whereas O⁻¹ is consumed at a time constant commensurate with the reaction rate, indicating that O⁻¹ drives the oxygen evolution reaction. These findings demonstrate the necessity of using multiple operando techniques to gain a unified understanding of the evolution of oxidation states and active sites with potential for water oxidation on oxide catalysts.

The oxidation state of an element is defined as the net charge an atom would have if all the bonding electrons in heteronuclear bonds were assigned to the more electronegative atom¹. It provides a straightforward way to understand and predict chemical bonding, redox reactions and materials properties. In practice, atoms in solids often share their electron densities because bonding is seldom purely ionic^{2,3}; it is generally heteropolar, exhibiting varying degrees of covalency and ionicity. Consequently, connecting oxidation states

to the observable electron density distribution in solid-state materials is often ambiguous.

In electrochemical systems, which inherently involve redox processes, assigning oxidation states and interpreting atomic charge can be complicated^{4,5}. In lithium batteries, for instance, the traditional view of transition-metal-centred redox processes for Li metal oxide cathodes has expanded to include oxygen redox processes within the oxide lattice, where oxygen may deviate from its conventional –2 oxide state

A full list of affiliations appears at the end of the paper. ✉e-mail: c.liang20@imperial.ac.uk; i.stephens@imperial.ac.uk; j.durrant@imperial.ac.uk; reshma.rao@imperial.ac.uk

and exist in a -1 state. However, whether this oxygen -1 state arises from localized O–O dimers, peroxo-like species or if it involves (de)localized holes on oxygen atoms within the metal oxide, remains under debate^{6–9}.

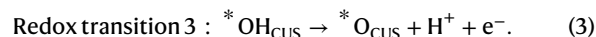
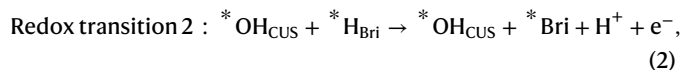
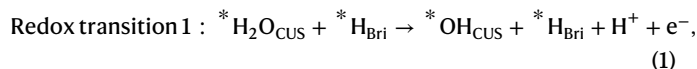
The complexities of determining oxidation states in electrocatalysts are even more pronounced. Unlike battery materials, where redox processes typically occur within the bulk, electrocatalytic reactions take place at the surface, where the local stoichiometry and electronic structure¹⁰ deviate from the bulk^{11–13}. The challenge of experimentally measuring surfaces at solid–liquid interfaces further complicates the assignment of active sites and species present¹⁴. Surface Pourbaix diagrams from density functional theory (DFT) calculations have enabled substantial progress in understanding the evolution of surface adsorbates; however, they do not provide a detailed picture of how charges are distributed between the metal and ligand sites^{15–17}.

Iridium oxides (IrO_x) have been extensively studied as water oxidation catalysts, since they exhibit both high activity¹⁸ and stability^{19,20} and serve as a model system for understanding solid–liquid interfaces^{21–23}, yet debate persists about the oxidation states under operating conditions and, more importantly, the active states that drive water oxidation. Operando X-ray absorption spectroscopy (XAS) and X-ray photoelectron spectroscopy studies have suggested the formation of Ir^{4+} (ref. 24), $\text{Ir}^{4.5+}$ (ref. 25) or Ir^{5+} species at oxygen evolution reaction (OER) potentials^{26–28}, whereas other reports propose Ir^{6+} (refs. 29,30). By contrast, recent near-edge X-ray absorption fine structure (NEXAFS) studies propose the formation of electrophilic oxygen species as key drivers for water oxidation^{31–34}. The assignment of electron-deficient oxygen is primarily based on a pre-edge feature, observed at -529 eV in the O K-edge spectra of iridium oxides. However, Klingenhof et al. assigned the -529 -eV signal to O ligands in the bulk after the α -to- γ transformation on NiX (X = Fe, Mn or Co) layer double hydroxide catalysts³⁵. Similarly, ref. 36 linked the 528–529-eV feature in $\text{H}_{3.6}\text{IrO}_4 \cdot 3.7\text{H}_2\text{O}$ to structural water, noting that removing water diminished the signal. For reference, liquid water absorbs at higher energies with the pre edge at -535 eV (refs. 37,38). A recent report suggested that the -529 -eV signal could be due to highly oxidized states of iridium, which shifts the absorption of oxygen due to the covalent Ir–O bond³⁹. Despite extensive operando studies, there remains no consensus on whether the key reactive species in IrO_x are metal centred (Ir^{n+}) or oxygen ligand centred (O-based holes), representing a long-standing mechanistic ambiguity in the field. This challenge arises from the inherent ambiguity of charge distribution during electrochemical oxidation processes, and is compounded by the fact that each spectroscopic technique offers only partial information, whereas a molecular view of the interface demands the combination of multiple operando techniques with a sufficient time resolution.

Here we combine multiple operando spectroscopies, mass spectrometry and theoretical methods to map the oxidation states of IrO_x and to identify and quantify the active oxidizing species that drive water oxidation. First, we use quantum mechanical calculations to probe the electron density distribution on surface atoms under varying potentials, linking these distributions to possible oxidation state changes. We then integrate operando optical spectroscopy (based on our recent work²²) with operando XAS at the Ir L edge and O K edge to track the oxidation state evolution of both metal centres and oxygen ligands. Time-resolved X-ray and optical spectroscopy are used to capture the dynamics of these states, illuminating their roles in the dynamic catalytic cycle. Using this multimodal, time-resolved approach, we demonstrate that surface oxidation at low potentials is dominated by the metal $5d$ states, whereas that at high potentials is dominated by the $\text{O}2p$ states, leading to the formation of electrophilic O^{-1} species. This species exhibits a time constant consistent with the overall reaction rate, suggesting its role as the key oxidizing species driving OER. These insights provide a detailed molecular view of the water oxidation interface, and demonstrate the importance of the covalent nature of metal oxide bonds in the formation of the active species for water oxidation.

Potential-dependent surface oxidation and localized charge density

On increasing the potential, changes in the surface oxygenated species can be predicted by surface Pourbaix diagrams (Fig. 1a and Supplementary Table 1), calculated using DFT. This result is consistent with previously established surface Pourbaix diagrams^{15,16,22,40–44}, and is not strongly influenced by the Hubbard U corrections for Ir d states (Supplementary Fig. 1). The changes in surface structures, related to redox transitions (also reported in our recent work²²) are (Fig. 1b and Supplementary Note 1)



CUS refers to coordinatively unsaturated Ir sites and Bri denotes bridge O sites bonded to two adjacent Ir atoms. To investigate the possible changes in charge density associated with these surface structural transitions, we calculated the average changes in Bader charges for surface Ir and O atoms during each redox transition (Fig. 1b, Supplementary Table 2 and Supplementary Fig. 2). Bader charges are obtained by dividing the electron density into atomic regions using surfaces at which the density gradient is zero. The results indicate substantial electron depletion predominantly occurring at Ir sites for redox transitions 1 and 2 (charge decreases of approximately -0.3e^- and -0.27e^- , respectively). Conversely, at higher potentials (redox transition 3), electron depletion is primarily observed on O atoms. Similar trends were observed for the (100) surface of hollandite IrO_2 , representative of a more open structure resembling amorphous IrO_x (refs. 22,45) (Supplementary Fig. 3). Furthermore, we calculated the evolution of the average Ir $5d$ and O $2p$ band centres of occupied states for surface atoms (Fig. 1c). As the potential increases, the O $2p$ band centre shifts upward from approximately -7.6 eV to around -3.8 eV, whereas the Ir $5d$ band centre shifts downward from approximately -3.9 eV to around -4.5 eV due to small changes in the Ir $5d$ band occupation near the Fermi level and changes in the overall shape of the Ir $5d$ band (Supplementary Fig. 4). Therefore, at lower potentials, oxidation depletes the electron density from the Ir $5d$ bands. As the potential increases, both Ir $5d$ and O $2p$ bands are close to the Fermi level, thereby initiating electron extraction from the O $2p$ bands (Fig. 1c, inset). These theoretical results suggest that oxidation on IrO_x may involve both Ir and O sites, and the dual-site participation in electron loss could complicate the assignment of oxidation states and the mechanistic understanding of water oxidation (Fig. 1a).

Determination of Ir and O oxidation using correlated spectroscopies

With theoretical evidence demonstrating that Ir and O could both be oxidized, we use a combination of operando optical (Fig. 2a), Ir L-edge (Fig. 2b) and O K-edge (Fig. 2c) spectroscopies to experimentally capture the changes in oxidation states. Electrodeposited IrO_x thin films are used considering they are volume active, that is, a majority of the Ir centres are active^{22,46}. Transmission electron microscopy analysis (Supplementary Note 2 and Supplementary Fig. 5) shows no evidence of crystallinity in these films, indicating that the material is composed of short-range ordered $[\text{IrO}_6]$ octahedra²². We note that this IrO_x is highly porous, with channels for electrolyte, in contrast to the long-range ordered rutile IrO_2 , which exhibits a more well-defined interface. Nevertheless, our previous optical spectroscopy studies have shown that

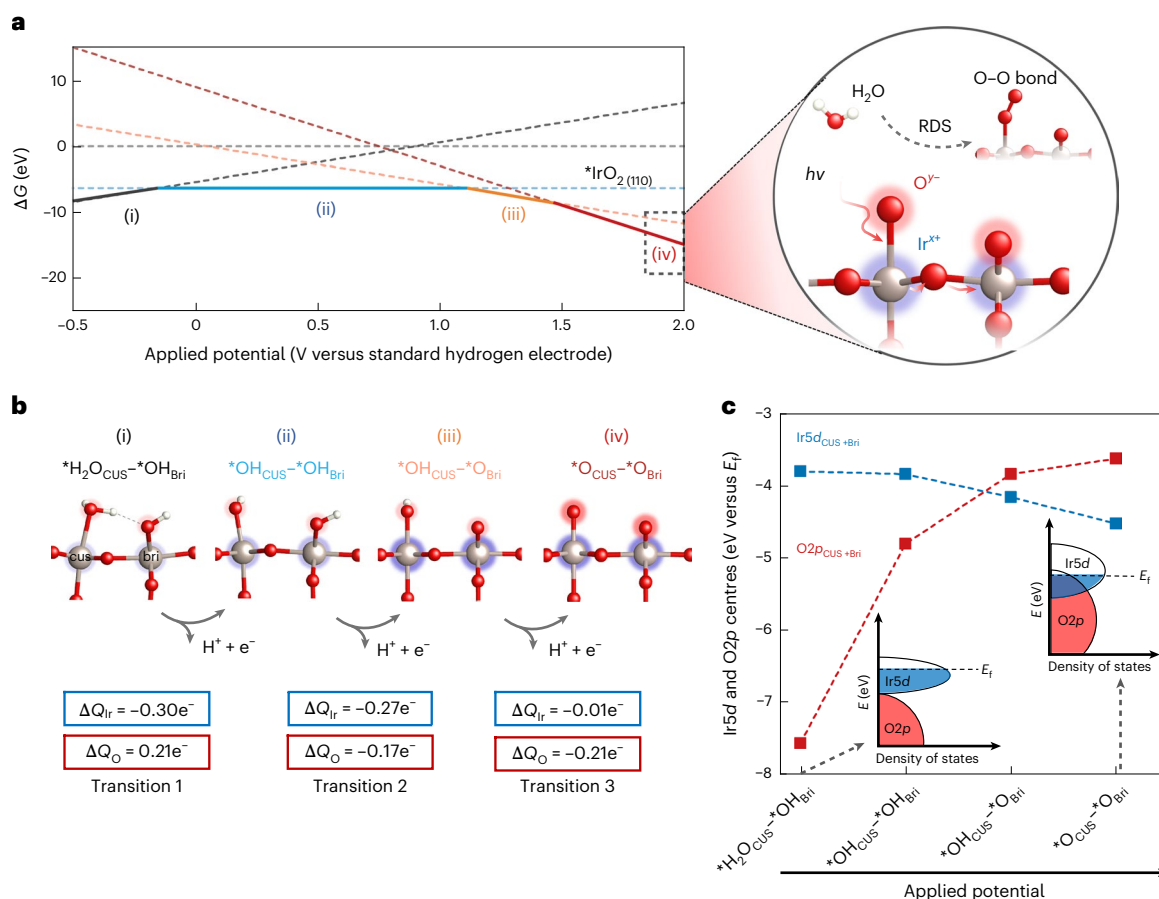


Fig. 1 | Evolution of surface intermediates, electronic structure and charge redistribution with potential on IrO_2 surfaces. **a**, Potential-dependent coverage of adsorbates on a modelled IrO_2 structure from DFT calculations (left) and schematic showing the calculated structure before the rate-determining step (RDS) of water oxidation and O–O bond formation, highlighting the ambiguous oxidation states and charge distribution for this critical intermediate (right). **b**, Structures involved in different redox transitions from DFT calculations and the corresponding sum of average change in Bader charges (ΔQ_{Ir} and ΔQ_{O}) for both CUS and bridge Ir and O atoms present at IrO_2 surfaces during each redox reaction. Positive (negative) numbers indicate an increase (decrease) in the

number of electrons (Supplementary Note 1 shows the detailed calculations). The blue and red shading surrounding the iridium and oxygen atoms are simple guides for the eye to indicate positive charge and negative charge, respectively, with the size and intensity of the shading reflecting the magnitude of charge change. **c**, Average $\text{Ir}5d$ and $\text{O}2p$ band centre energies of the occupied states (versus the Fermi level E_f) of surface atoms for different surface adsorbate structures (Supplementary Fig. 2 shows the separated band centres of CUS and Bri sites). The inset scheme illustrates the overlapping of $\text{Ir}5d$ with $\text{O}2p$ bands as the surface structure evolves with increasing applied potential and the upshift of $\text{O}2p$ bands (Supplementary Note 1 shows the projected density of states).

these materials share similar redox chemistry, although amorphous IrO_x exhibits a much higher density of accessible sites for redox transitions and OER²². Recent studies have also shown comparable changes in $\text{Ir}4f$ X-ray photoelectron spectroscopy as well as the OK-edge and $\text{Ir}L_3$ -edge XAS spectra for amorphous and crystalline iridium oxides^{26,47}, suggesting that the observation on amorphous IrO_x could reasonably extend to rutile systems.

Operando optical spectroscopy shows an increase in absorbance with potential (Fig. 2a). Following our previous work, these can be deconvoluted into three different redox transitions according to their spectral shape, and their densities are quantified using the Lambert–Beer law (light blue, orange and red lines in Fig. 2d, black y axis; Supplementary Note 3 and Supplementary Figs. 6–8 provide the deconvolution details)^{21,22}. Similarly, operando $\text{Ir}L$ -edge XANES shows that the white-line position continuously shifts to a higher energy with increasing potential from 0.6 V to $-1.4\text{ V}_{\text{RHE}}$ (Fig. 2b, adapted from our previous work²¹), but remains roughly unchanged at higher potentials. This energy shift corresponds to an increase in the average iridium oxidation state from approximately +3.1 to around +4.7 (Fig. 2d, blue triangles). Interestingly, the potential dependence of the first two redox transitions detected via optical spectroscopy correlate well with the increase in Ir oxidation state (that is, the light blue lines and orange

line overlap well with the blue triangles), thereby corresponding to the oxidation of Ir^{3+} to Ir^{4+} and then Ir^{4+} to Ir^{5+} . Although the average Ir oxidation state is +4.7, the redox active sites are probably Ir^{5+} with a minor fraction of Ir^{3+} and Ir^{4+} . This is consistent with recent reports showing that IrO_x attains a surface oxidation state of Ir^{5+} at OER-relevant potentials²⁶. Crucially, the final redox transition observed in optical spectroscopy, occurring in the OER region, does not correspond to further oxidation of the Ir centre. Instead, as the Ir oxidation state plateaus, redox transition 3 emerges (Fig. 2d, red lines). This observation suggests that there is an additional oxidation process in which electrons are extracted without further oxidizing Ir. We note that the above-mentioned spectroscopic changes are reversible with potential, and no substantial changes are observed in the electrochemistry (Supplementary Fig. 9), crystallinity (Supplementary Figs. 10 and 11), surface composition (Supplementary Fig. 12) or optical spectroscopy measurements after 20 cycles (Supplementary Fig. 13; Supplementary Note 4 provides a detailed discussion).

To further understand the physicochemical nature of the final redox transition, operando NEXAFS was used to examine changes in the oxygen ligands (Supplementary Note 5 and Supplementary Fig. 14). The operando O K-edge spectra resemble those of pure water (Fig. 2c, inset)^{37,38} but display distinct features in the low-energy region from

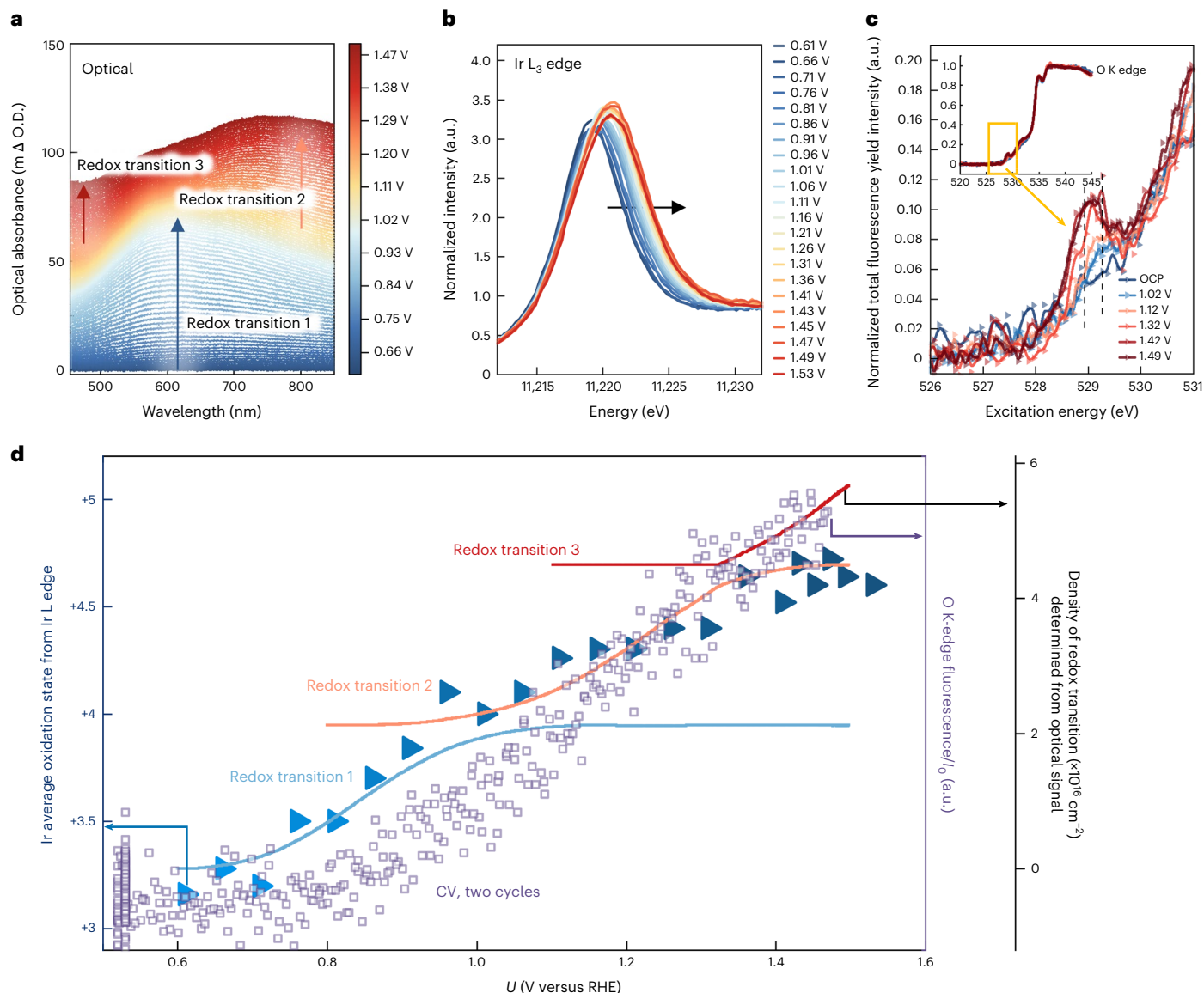


Fig. 2 | Correlating optical, hard and soft X-ray spectroscopies to identify Ir and O oxidation processes. **a**, Difference ultraviolet–visible absorbance spectra of IrO_x during a linear sweep scan from 0.66 V_{RHE} to 1.48 V_{RHE} in 0.1-MHClO₄ at a scan rate of 1 mV s⁻¹ (iR corrected). The absorption changes are calculated with respect to the absorption at 0.66 V_{RHE}. Absorption changes were recorded after five cyclic voltammetry cycles, at every 1 mV and shown at every 5 mV. Arrows indicate the dominant wavelengths at which the absorbance increases with potential, representing three different redox transitions. **b**, Ir L₃-edge XANES spectra of electrodeposited IrO_x on FTO substrate measured at different potentials in 0.1-MHClO₄. Data adapted from our previous work²¹. **c**, Insets: steady-state operando NEXAFS O K-edge spectra of amorphous IrO_x deposited

on gold-coated SiN_x substrates measured at various applied potentials in 0.1-M HClO₄ electrolyte. Potential values are given versus a reversible hydrogen electrode (RHE). The data are normalized to the intensity at around 540 eV and calibrated using the pre edge of water at 535 eV (refs. 37,38). The main figure shows a zoomed-in view with energy ranging from 526 to 531 eV. Dashed lines show two peak positions at an increase of around 528.9 eV and 529.3 eV with the applied potentials. **d**, Comparison between the iridium oxidation state determined from the white-line position in **b** (left y-axis), the sum of deconvoluted densities of redox transitions 1, 2 and 3 from optical spectroscopy (black, right y-axis) and the fluorescence intensity at 529 eV in the O K edge over two cyclic voltammetry cycles. The y-axis scales are adjusted for visual clarity.

527 eV to 532 eV associated with IrO_x (Fig. 2c and Supplementary Figs. 15 and 16). With increasing potential from the open-circuit potential (OCP) to 1.49 V_{RHE}, there is an increase in intensity between 528.5 and 530 eV. This observation aligns with findings from refs. 31–34 on IrO_x and refs. 35,48,49 on Ni-Fe based catalysts. It is worth noting that assigning O K-edge features is not straightforward, as the absorption energies of oxygen species can vary across metal oxides^{32,34,36,39,50}. Considering this challenge, rather than assigning specific peaks to different species, we traced the signal at 529 eV with potential during two cyclic voltammetry cycles from 0.5 V_{RHE} to -1.47 V_{RHE} (Fig. 2d, purple dots), and correlated it with the Ir oxidation states and optically resolved redox transitions (Supplementary Fig. 17). The oxygen XAS signal remains

constant in the low-potential range (0.5–0.85 V_{RHE}), but increases continuously at a higher potential up to 1.47 V_{RHE}. In particular, the increase in XAS signal to >1.40 V_{RHE} aligns well with redox transition 3 resolved in optical spectroscopy.

The above correlated spectroscopic results suggest that the electrons extracted during the final redox transition might come from oxygen ligands, forming electron-deficient oxygen species O⁻¹. In addition, the increase in the oxygen XAS signal during redox transition 2 is attributed to changes in the signal of different oxygenated species (that is, *OH_{Bri} → *O_{Bri} + H⁺ + e⁻). The oxygen involved in redox transition 2 probably remains in a chemical state close to typical O⁻², as the observed charge extraction is primarily accounted for by changes in

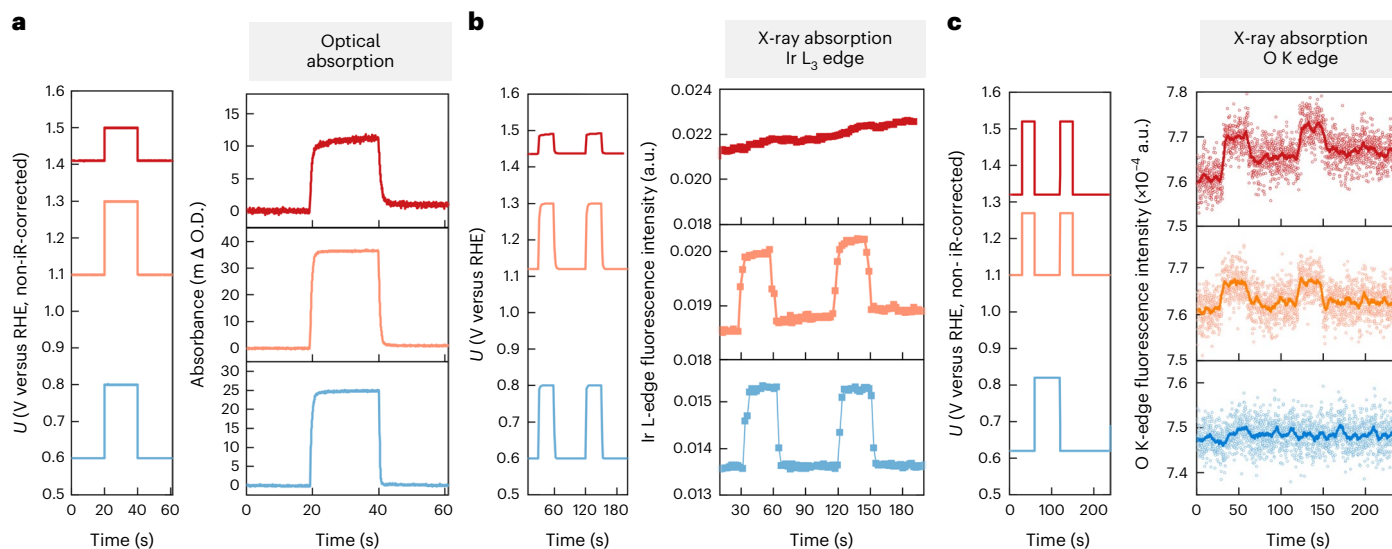


Fig. 3 | Dynamics of Ir and O oxidation probed by time-resolved operando optical and X-ray spectroscopies. a, Time-resolved optical absorption changes during potential step experiments on IrO_x in 0.1-M HClO_4 electrolyte. Potentials (non-iR-corrected) were stepped from 0.6 to 0.8 V_{RHE} , 1.1 to 1.3 V_{RHE} and 1.41 to 1.5 V_{RHE} . Optical absorption was monitored at wavelengths of 600 nm, 800 nm and 500 nm, corresponding to the maximum absorption wavelength for redox transitions 1, 2 and 3, respectively (Supplementary Fig. 7). **b**, Changes in fluorescence intensity at the Ir L_3 edge (11,222 eV) during potential step experiments on IrO_x deposited on an FTO substrate in 0.1-M HClO_4 electrolyte.

Potential steps were applied between 0.6 and 0.8 V_{RHE} , 1.12 and 1.3 V_{RHE} and 1.44 and 1.5 V_{RHE} , corresponding to redox transitions 1, 2 and 3, respectively, as identified from the spectral deconvolution in optical spectroscopy. **c**, Changes in the fluorescence intensity at the O K edge during potential step experiments in 0.1-M HClO_4 electrolyte. Potentials (non-iR-corrected) were stepped in the ranges of 0.62–0.82 V_{RHE} , 1.1–1.27 V_{RHE} and 1.32–1.52 V_{RHE} . Fluorescence intensity changes were monitored at 529 eV for the potential ranges of 0.62–0.82 V_{RHE} and 1.1–1.27 V_{RHE} , and at 528.7 eV for the range of 1.32–1.52 V_{RHE} .

the Ir oxidation states. Thus, by comparing Ir and O signals with optical spectroscopy, our results seem to support the existence of O^{-1} at positive potentials. However, steady-state XAS measurements have limited dynamic and potential resolution, and are susceptible to beam damage or time-dependent changes during prolonged exposure⁹, which may introduce uncertainties. Therefore, we next traced the dynamic responses of Ir and O to applied potential using time-resolved optical and X-ray spectroscopies.

Dynamics of iridium and oxygen oxidation

The dynamic responses of the optical, Ir and oxygen XAS signals are tracked as the potential steps up and down in different potential ranges. The ranges 0.6–0.8 V_{RHE} , 1.1–1.3 V_{RHE} and 1.4–1.5 V_{RHE} were selected for redox transitions 1, 2 and 3, respectively (Fig. 2d). As shown in Fig. 3a, for all three redox transitions, the optical absorption signal responds rapidly to the potential change. Similarly, the Ir XAS intensity at 11,222 eV rises and falls with the stepping up and down of potential in the ranges corresponding to redox transitions 1 and 2 (Fig. 3b).

The Ir XAS intensity at 11,222 eV is proportional to its oxidation states changes, as established by correlating the intensity with the oxidation states obtained in Fig. 2d (Supplementary Note 6 and Supplementary Figs. 18 and 19). By contrast, during redox transition 3 (1.44–1.5 V_{RHE}), the Ir XAS signal does not respond to potential changes; instead, a very slow and gradual increase in the oxidation state over time was observed (Fig. 3b, top). This difference between the time-resolved optical and Ir L_3 -edge XAS spectroscopies suggests that although redox transitions 1 and 2 are associated with the oxidation of iridium, the third transition is not.

The observed slow increase in fluorescence intensity over time could indicate the time-dependent oxidation of a small amount of bulk iridium, inaccessible within shorter experimental time frames. Similar measurements on the dynamics of oxygen species reveal that the fluorescence intensity at 529 eV does not change from 0.62 to 0.82 V_{RHE} , but changes with potential steps in the ranges of 1.1–1.27 V_{RHE} and 1.32–1.52 V_{RHE} (Fig. 3c). This behaviour aligns with the changes

observed during cyclic voltammetry cycles (Fig. 2c). Further investigations establish that the observed changes are indeed sensitive to the selected X-ray beam energy (Supplementary Fig. 20), confirming that the changes are related to alterations in the oxygen species.

On the basis of experimental and DFT findings, the first redox transition is attributed to the Ir^{3+} to Ir^{4+} transition and a deprotonation of water into $^*\text{OH}$ on the Ir CUS site. This is consistent with recent findings suggesting that $^*\text{OH}$ on the CUS Ir site is hardly visible in the O K-edge NEXAFS⁴⁷. The second redox transition can be associated with further oxidation from Ir^{4+} towards Ir^{5+} , accompanied by the deprotonation of $^*\text{OH}$ on the bridge site into $^*\text{O}$. This $^*\text{OH}$ to $^*\text{O}$ transformation was captured by the absorption peak at around 529.3 eV in O K-edge NEXAFS spectra^{23,27,31–34,47–49}. The final redox transition, occurring in the OER-relevant potential region, involves further oxidation and the deprotonation of $^*\text{OH}$ at the CUS site to form $^*\text{O}^{-1}$, whereas Ir remains as Ir^{5+} . This is consistent with our DFT calculations showing that electron depletion in this step is dominated by the oxygen ligand. This assignment differs from oxygen redox that emphasizes lattice oxygen involvement, such as anion redox in battery cathodes and lattice oxygen evolution mechanism in OER⁵¹. In addition, our results do not support the accumulation of a substantial coverage of higher oxidation state Ir^{6+} species in these materials, consistent with a recent report showing gas-phase IrO_3 (Ir^{6+}) only occurs as a degradation side product in rutile IrO_2 (ref. 52).

Kinetics of O^{-1} species for water oxidation

Although we have established that oxidizing species Ir^{5+} and O^{-1} co-exist at high potentials, it remains unclear whether Ir^{5+} , O^{-1} or a cooperative interaction between them controls the rate-determining O–O-bond-forming step. To investigate the roles of these species in catalysing water oxidation, we determined their decay time constants by coupling the OCP decay measurements with time-resolved optical and X-ray spectroscopies. In this method, the potential is stepped up and held before switching to an open circuit, allowing the electrode to relax (Fig. 4a). Figure 4b shows that across all three potential regions

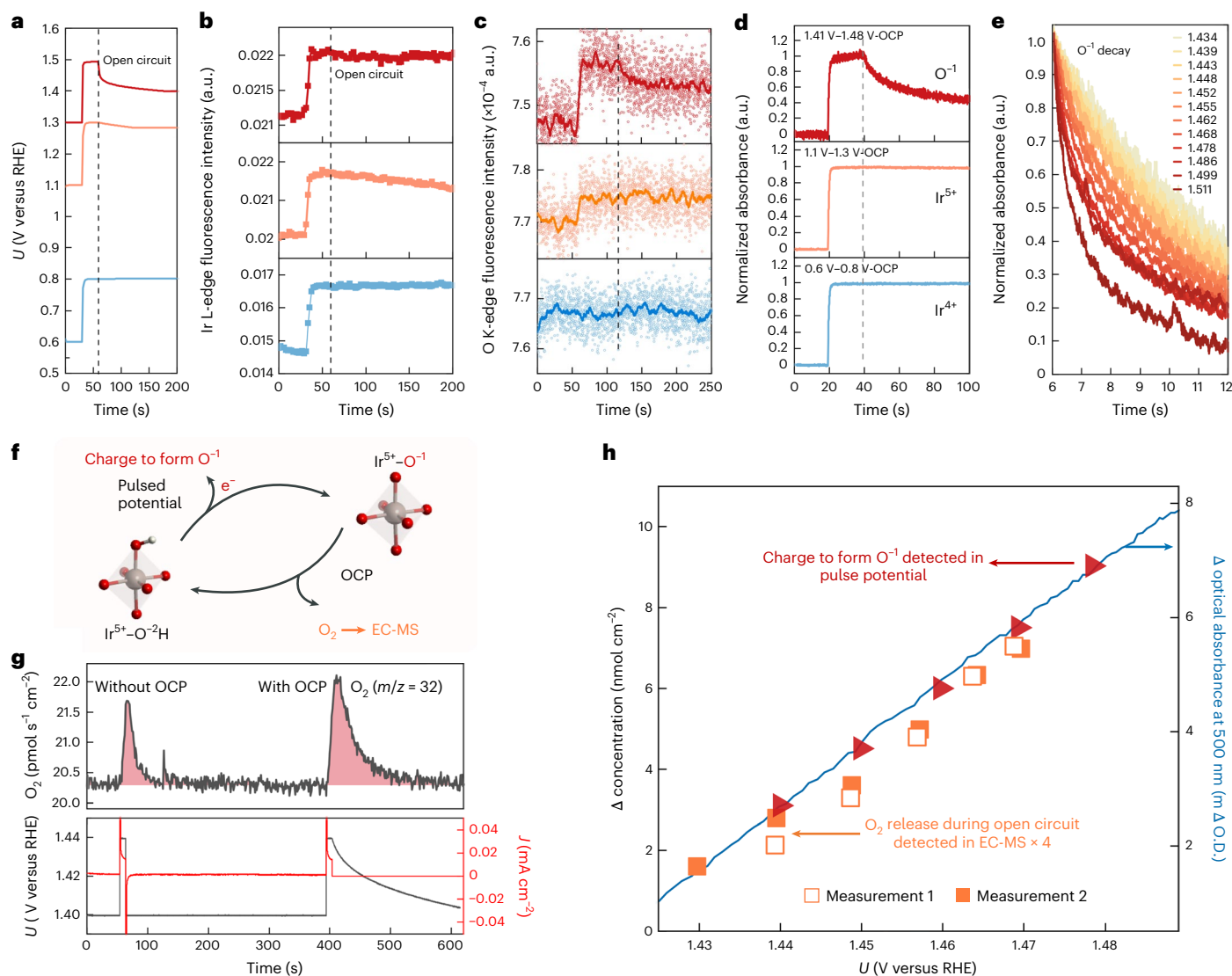


Fig. 4 | Operando tracking of O⁻¹ and their decay to molecular oxygen during OCP. **a**, Potential profile of OCP decay measurement between 0.6 and 0.8 V_{RHE}, 1.12 and 1.3 V_{RHE}, and 1.3 and 1.5 V_{RHE} in 0.1-M HClO₄ electrolyte. **b**, Change in fluorescence intensity of Ir L edge (11,222 eV). **c**, Change in fluorescence intensity of O K edge during OCP decay measurement between 0.62 and 0.82 V_{RHE} and 1.1 and 1.27 V_{RHE} at 529 eV, and 1.27 and 1.52 V_{RHE} at 528.7 eV. **d**, Normalized optical absorption decay. The optical signals are taken at the maximum absorption wavelength for each redox transition, with redox transition forming Ir⁴⁺ at 600 nm, Ir⁵⁺ at 800 nm and O⁻¹ at 500 nm (Fig. 2a and Supplementary Note 3 show the spectra). **e**, Normalized optical signal decay at 500 nm at different applied potentials. The potentials are iR corrected and in the RHE scale. **f**, Schematic showing the formation of O⁻¹ on removing an electron and proton from a protonated IrO₆ structure by raising the potentials and its corresponding decay during OCP to form molecular oxygen. **g**, O₂ (m/z = 32) detected in EC-MS for pulsed potential measurements from 1.40 to 1.44 V_{RHE} and for a subsequent

OCP decay measurement with the same pulsed potential steps and holding time. **h**, Quantitative comparison between the charge associated with O⁻¹ formation and the detected molecular oxygen during OCP decay. The amount of O⁻¹ formed is quantified by integrating the cathodic current peak during pulsed potential measurements, corresponding to the reduction of accumulated O⁻¹ back to O⁻² at 1.415 V_{RHE}, assuming a one-to-one correspondence between O⁻¹ formation and the number of electrons transferred. Above this potential, the charge is dominated by oxygen redox with negligible contribution from iridium (Fig. 2d), and double-layer charging/discharging is minor (Supplementary Note 7 and Supplementary Fig. 28). The amount of O₂ released during OCP decay is directly measured by EC-MS, with contributions from potential-jumping controls subtracted (Supplementary Figs. 24 and 27). The change in optical absorption relative to 1.415 V_{RHE} at 500 nm (right axis) is co-plotted to correlate O⁻¹ accumulation with the corresponding optical signal changes resulting from redox transitions.

examined, the XAS intensity of Ir remains stable after switching to the open circuit, indicating that the accumulated Ir⁴⁺ and Ir⁵⁺ species are stable. By contrast, the oxygen XAS signals at higher potentials (1.32 to 1.52 V_{RHE})—assigned to O⁻¹ species—exhibit a notable decay, suggesting the consumption of these oxygen species during open-circuit conditions (Fig. 4c). These dynamic behaviours of iridium and oxygen species were also clearly observed using time-resolved optical spectroscopy (Fig. 4d). We note that the loss of spectral features during the initial decay closely matches those associated with redox transition 3, which generates O⁻¹ species (Supplementary Fig. 21). In addition, the initial

decay rate increases with the applied potential (Fig. 4e), with the time required for the initial 25% decay decreasing from approximately 7 s at 1.43 V to 0.9 s at 1.51 V_{RHE}, indicating a quicker consumption of O⁻¹ species at higher potentials and at higher coverages of O⁻¹. Similar decay trends were observed in time-resolved O K edge absorption spectroscopy (Supplementary Fig. 22). The stark difference in the behaviour of highly oxidized Ir species and electron-deficient O⁻¹ species, as evidenced by both optical and X-ray spectroscopies, suggests that Ir-oxidizing species does not change the oxidation state under OER conditions; instead, O⁻¹ is dynamically changing. These results suggest that the fast

kinetics of O–O bond formation and oxygen molecule release on IrO_x can be attributed to the accumulation of O⁻¹ species at high potentials, resulting from the high covalency of Ir–O on oxidation (Fig. 4f), thereby supporting the notion that O⁻¹ species drive water oxidation^{23,28,31–34}.

To further understand the correlation between O⁻¹ and oxygen evolution, we quantified oxygen release during OCP decay using highly sensitive (resolution, subpicomole per second) on-chip electrochemical mass spectrometry (EC-MS)⁵³. Oxygen signals were measured using two sequential procedures: an OCP decay measurement and a step potential measurement as control (Supplementary Note 7). In particular, the OCP decay measurement shows a larger oxygen signal compared with the step potential measurement, indicating additional oxygen release during open-circuit decay (Fig. 4g). Reversing the order of the two procedures yielded consistent results (Supplementary Fig. 23). Measurements at potentials from 1.44 to 1.48 V_{RHE} conducted in two independent experiments, consistently showed increased oxygen release during OCP, which was quantified (Supplementary Note 7 and Supplementary Figs. 24–26). Interestingly, the net amount of oxygen produced during OCP decay shows an almost-linear increase with the applied potential before switching to the open circuit. A similar linear increase is observed in the 500-nm absorbance signal and the accumulation of O⁻¹ species (Fig. 4h; Supplementary Fig. 27 shows the quantification of O⁻¹). In particular, the O⁻¹ concentration is almost four times the amount of oxygen released during OCP decay, which suggests that the release of every O₂ from the water molecules gives rise to four electrons to discharge four accumulated O⁻¹ species. These results indicate that the consumption of O⁻¹ is quantitatively linked to the release of oxygen during open-circuit decay, suggesting that the O⁻¹ species could be involved in the step of forming the O–O bond and subsequent oxygen release. In addition, inductively coupled plasma mass spectrometry measurements show that Ir dissolution during decay is 2–3 orders of magnitude lower than the amount of oxygen released (Supplementary Fig. 29 and Supplementary Note 8), indicating that dissolution is a minor contribution. On the basis of previous established DFT calculations for IrO₂(110) surfaces—which suggest that the transition from *O to *OOH (that is, the O–O bond formation) is the rate-determining step^{22,23,40,41}—we propose a mechanism for the open-circuit decay process, analogous to our previous work²². In this process, an active state (O⁻¹) undergoes a nucleophilic attack by a water molecule, leading to O–O bond formation and subsequent oxygen release. To maintain charge balance without external electron transfer (as that during open-circuit conditions), other O⁻¹ species in the network accept a proton and become reduced, regenerating O⁻² in the form of *OH on the surface. Although this mechanism is specific to the OCP decay, it involves a fundamental catalytic cycle with charged surface oxygen species (O⁻¹), water molecules, O–O bond formation and oxygen release. The key distinction between OCP decay and constant potential operation is the presence of an externally applied potential during the latter, which facilitates continuous electron extraction from the catalyst. This external potential enables the rapid reoxidation of reduced O⁻² sites back to O⁻¹ species, allowing them to participate in successive catalytic cycles releasing O₂. Therefore, we consider the mechanism described for OCP decay representing a single catalytic cycle of the OER on iridium oxides.

Under anodic polarization, the progressive oxidation of Ir enhances Ir–O covalency and brings the Ir5d and O2p band centres into closer energetic alignment, thereby promoting electron depletion from surface oxygen atoms and enabling the formation of O⁻¹ species necessary for driving O–O bond formation. The ability of iridium oxides to stabilize such electron-deficient oxygen states may arise from the unique covalency of surface Ir–O bonds under high potentials—a property that may be fundamental to their exceptionally fast OER kinetics. Further analysis of reaction rate versus O⁻¹ concentrations suggests that IrO_x is unlikely to follow a simple rate law kinetics since we observed an unphysically high reaction order (Supplementary Fig. 30

and Supplementary Note 9); instead, our data align better with a kinetic model in which the reaction rate increases approximately exponentially with the accumulation of O⁻¹ species. These results agree with previous reports, which suggest that repulsive interactions exist between oxo species and lower the activation barrier of the rate-determining step and, thus, promote water oxidation^{21–23,54}. Future work should also directly probe whether the accumulation of O⁻¹ species influences dissolution, opening up pathways to jointly optimize the OER activity and stability. As these reactive O⁻¹ configurations are accessible only under operando conditions, our results underscore that an accurate understanding of catalytic activity should account for the electronic structure of the oxidized surface under very positive potential, rather than relying solely on bulk stoichiometric models. As a result, future research focused on tuning surface metal–oxygen covalency and band alignment at high potentials can open promising avenues for the design of more active OER catalysts.

Conclusions

In summary, we used multimodal, time-resolved spectroscopies to elucidate the potential-dependent oxidation states of iridium and oxygen in iridium oxide and its impact on water oxidation. We found a sequential oxidation process, which first involves iridium oxidation (Ir³⁺/Ir⁴⁺ and Ir⁴⁺/Ir⁵⁺) at low potentials, followed by electron depletion from oxygen ligands at higher potentials, primarily due to the increased covalency of Ir–O, leading to the formation of electrophilic O⁻¹ at OER potentials. Time-resolved spectroscopies show that the lifetime of oxidized iridium (Ir⁵⁺) is much longer than the time constant of oxygen release, whereas the kinetics of electrophilic oxygen O⁻¹ align closely with OER. These suggest that electrophilic oxygen, rather than the highly oxidized iridium, plays a key role in driving the rate-determining-step O–O bond formation. EC-MS results show that the concentration of O⁻¹ species is quantitatively correlated to the amount of molecular oxygen released, with the consumption of roughly four O⁻¹ for the release of every oxygen molecule. These results provide a unified mechanistic picture that resolves long-standing discrepancies over whether Ir-centred or oxygen-ligand-centred species act as the reactive oxidants during water oxidation. Our results also demonstrate the necessity of multimodal, time-resolved characterization techniques to gain a holistic understanding of complex solid–liquid interfaces. Beyond OER on metal oxides, identifying potential-dependent oxidation states and their dynamics serves as an important tool to determine how charge transfer occurs during rate-determining catalytic steps for a number of reactions such as CO₂ reduction and oxygen reduction.

Online content

Any methods, additional references, Nature Portfolio reporting summaries, source data, extended data, supplementary information, acknowledgements, peer review information; details of author contributions and competing interests; and statements of data and code availability are available at <https://doi.org/10.1038/s41563-026-02514-9>.

References

- McNaught, A. D. & Wilkinson, A. *Compendium of Chemical Terminology* (Blackwell Science, 1997).
- Walsh, A., Sokol, A. A., Buckeridge, J., Scanlon, D. O. & Catlow, C. R. A. Oxidation states and ionicity. *Nat. Mater.* **17**, 958–964 (2018).
- Walsh, A., Sokol, A. A., Buckeridge, J., Scanlon, D. O. & Catlow, C. R. A. Electron counting in solids: oxidation states, partial charges, and ionicity. *J. Phys. Chem. Lett.* **8**, 2074–2075 (2017).
- Kuznetsov, D. A. et al. Tuning redox transitions via inductive effect in metal oxides and complexes, and implications in oxygen electrocatalysis. *Joule* **2**, 225–244 (2018).
- Luo, K. et al. Charge-compensation in 3d-transition-metal-oxide intercalation cathodes through the generation of localized electron holes on oxygen. *Nat. Chem.* **8**, 684–691 (2016).

6. Marie, J.-J. et al. Trapped O₂ and the origin of voltage fade in layered Li-rich cathodes. *Nat. Mater.* **23**, 818–825 (2024).
7. Sathiyaraj, M. et al. Reversible anionic redox chemistry in high-capacity layered-oxide electrodes. *Nat. Mater.* **12**, 827–835 (2013).
8. Assat, G. & Tarascon, J.-M. Fundamental understanding and practical challenges of anionic redox activity in Li-ion batteries. *Nat. Energy* **3**, 373–386 (2018).
9. Gao, X. et al. Clarifying the origin of molecular O₂ in cathode oxides. *Nat. Mater.* **24**, 743–752 (2025).
10. Lunger, J. R. et al. Towards atom-level understanding of metal oxide catalysts for the oxygen evolution reaction with machine learning. *npj Comput. Mater.* **10**, 80 (2024).
11. Haase, F. T. et al. Role of Fe decoration on the oxygen evolving state of Co₃O₄ nanocatalysts. *Energy Environ. Sci.* **17**, 2046–2058 (2024).
12. Hubert, M. A. et al. Characterization of a dynamic Y₂Ir₂O₇ catalyst during the oxygen evolution reaction in acid. *J. Phys. Chem. C* **126**, 1751–1760 (2022).
13. Yang, F. et al. Dynamics of bulk and surface oxide evolution in copper foams for electrochemical CO₂ reduction. *Commun. Chem.* **7**, 66 (2024).
14. Suntivich, J. et al. Probing intermediate configurations of oxygen evolution catalysis across the light spectrum. *Nat. Energy* **9**, 1191–1198 (2024).
15. Rossmeisler, J., Qu, Z. W., Zhu, H., Kroes, G. J. & Nørskov, J. K. Electrolysis of water on oxide surfaces. *J. Electroanal. Chem.* **607**, 83–89 (2007).
16. Man, I. C. et al. Universality in oxygen evolution electrocatalysis on oxide surfaces. *ChemCatChem* **3**, 1159–1165 (2011).
17. Nørskov, J. K. et al. Origin of the overpotential for oxygen reduction at a fuel-cell cathode. *J. Phys. Chem. B* **108**, 17886–17892 (2004).
18. McCrory, C. C. L., Jung, S., Peters, J. C. & Jaramillo, T. F. Benchmarking heterogeneous electrocatalysts for the oxygen evolution reaction. *J. Am. Chem. Soc.* **135**, 16977–16987 (2013).
19. Geiger, S. et al. The stability number as a metric for electrocatalyst stability benchmarking. *Nat. Catal.* **1**, 508–515 (2018).
20. Cherevko, S. et al. Oxygen and hydrogen evolution reactions on Ru, RuO₂, Ir, and IrO₂ thin film electrodes in acidic and alkaline electrolytes: a comparative study on activity and stability. *Catal. Today* **262**, 170–180 (2016).
21. Liang, C. et al. Role of electrolyte pH on water oxidation for iridium oxides. *J. Am. Chem. Soc.* **146**, 8928–8938 (2024).
22. Liang, C. et al. Unravelling the effects of active site density and energetics on the water oxidation activity of iridium oxides. *Nat. Catal.* **7**, 763–775 (2024).
23. Nong, H. N. et al. Key role of chemistry versus bias in electrocatalytic oxygen evolution. *Nature* **587**, 408–413 (2020).
24. Saveleva, V. A. et al. Operando evidence for a universal oxygen evolution mechanism on thermal and electrochemical iridium oxides. *J. Phys. Chem. Lett.* **9**, 3154–3160 (2018).
25. Hillman, A. R., Skopek, M. A. & Gurman, S. J. X-ray spectroscopy of electrochemically deposited iridium oxide films: detection of multiple sites through structural disorder. *Phys. Chem. Chem. Phys.* **13**, 5252–5263 (2011).
26. Diklić, N. et al. Surface Ir⁺⁵ formation as a universal prerequisite for O₂ evolution on Ir oxides. *ACS Catal.* **13**, 11069–11079 (2023).
27. Nong, H. N. et al. A unique oxygen ligand environment facilitates water oxidation in hole-doped IrNiO_x core-shell electrocatalysts. *Nat. Catal.* **1**, 841–851 (2018).
28. Velasco-Vélez, J.-J. et al. Surface electron-hole rich species active in the electrocatalytic water oxidation. *J. Am. Chem. Soc.* **143**, 12524–12534 (2021).
29. Li, A. et al. Atomically dispersed hexavalent iridium oxide from MnO₂ reduction for oxygen evolution catalysis. *Science* **384**, 666–670 (2024).
30. Retuerto, M. et al. Highly active and stable OER electrocatalysts derived from Sr₂MlIrO₆ for proton exchange membrane water electrolyzers. *Nat. Commun.* **13**, 7935 (2022).
31. Pfeifer, V. et al. The electronic structure of iridium and its oxides. *Surf. Interface Anal.* **48**, 261–273 (2016).
32. Pfeifer, V. et al. The electronic structure of iridium oxide electrodes active in water splitting. *Phys. Chem. Chem. Phys.* **18**, 2292–2296 (2016).
33. Pfeifer, V. et al. Reactive oxygen species in iridium-based OER catalysts. *Chem. Sci.* **7**, 6791–6795 (2016).
34. Pfeifer, V. et al. In situ observation of reactive oxygen species forming on oxygen-evolving iridium surfaces. *Chem. Sci.* **8**, 2143–2149 (2017).
35. Klingenhof, M. et al. High-performance anion-exchange membrane water electrolyzers using NiX (X = Fe, Co, Mn) catalyst-coated membranes with redox-active Ni–O ligands. *Nat. Catal.* **7**, 1213–1222 (2024).
36. Zhang, R. et al. First example of protonation of Ruddlesden–Popper Sr₂IrO₄: a route to enhanced water oxidation catalysts. *Chem. Mater.* **32**, 3499–3509 (2020).
37. Wernet, P. et al. The structure of the first coordination shell in liquid water. *Science* **304**, 995–999 (2004).
38. Myneni, S. et al. Spectroscopic probing of local hydrogen-bonding structures in liquid water. *J. Phys. Condens. Matter* **14**, L213 (2002).
39. Frati, F., Hunault, M. O. J. Y. & de Groot, F. M. F. Oxygen K-edge X-ray absorption spectra. *Chem. Rev.* **120**, 4056–4110 (2020).
40. Ping, Y., Nielsen, R. J. & Goddard, W. A. III The reaction mechanism with free energy barriers at constant potentials for the oxygen evolution reaction at the IrO₂ (110) surface. *J. Am. Chem. Soc.* **139**, 149–155 (2017).
41. Dickens, C. F., Kirk, C. & Nørskov, J. K. Insights into the electrochemical oxygen evolution reaction with ab initio calculations and microkinetic modeling: beyond the limiting potential volcano. *J. Phys. Chem. C* **123**, 18960–18977 (2019).
42. Kuo, D. Y. et al. Influence of surface adsorption on the oxygen evolution reaction on IrO₂(110). *J. Am. Chem. Soc.* **139**, 3473–3479 (2017).
43. Tripathi, A., Ocampo-Restrepo, V. K., Nørskov, J. K. & Kastlunger, G. Field effects explain the unintuitive potential response of electrochemical oxygen evolution in acid. *RSC Sustain.* **3**, 2659–2668 (2025).
44. Kwon, S. et al. Facet-dependent oxygen evolution reaction activity of IrO₂ from quantum mechanics and experiments. *J. Am. Chem. Soc.* **146**, 11719–11725 (2024).
45. Willinger, E., Massué, C., Schlögl, R. & Willinger, M. G. Identifying key structural features of IrO_x water splitting catalysts. *J. Am. Chem. Soc.* **139**, 12093–12101 (2017).
46. Petit, M. A. & Plichon, V. Anodic electrodeposition of iridium oxide films. *J. Electroanal. Chem.* **444**, 247–252 (1998).
47. Mom, R. V. et al. Operando structure–activity–stability relationship of iridium oxides during the oxygen evolution reaction. *ACS Catal.* **12**, 5174–5184 (2022).
48. Drevon, D. et al. Uncovering the role of oxygen in Ni-Fe(O_xH_y) electrocatalysts using in situ soft X-ray absorption spectroscopy during the oxygen evolution reaction. *Sci. Rep.* **9**, 1532 (2019).
49. van der Heijden, O., Park, S., Eggebeen, J. J. & Koper, M. T. M. Non-kinetic effects convolute activity and Tafel analysis for the alkaline oxygen evolution reaction on NiFeOOH electrocatalysts. *Angew. Chem. Int. Ed.* **62**, e202216477 (2023).
50. Suntivich, J. et al. Estimating hybridization of transition metal and oxygen states in perovskites from O K-edge X-ray absorption spectroscopy. *J. Phys. Chem. C* **118**, 1856–1863 (2014).

51. Grimaud, A., Hong, W. T., Shao-Horn, Y. & Tarascon, J. M. Anionic redox processes for electrochemical devices. *Nat. Mater.* **15**, 121–126 (2016).
52. Kasian, O., Grote, J.-P., Geiger, S., Cherevko, S. & Mayrhofer, K. J. J. The common intermediates of oxygen evolution and dissolution reactions during water electrolysis on iridium. *Angew. Chem. Int. Ed.* **57**, 2488–2491 (2018).
53. Scott, S. B. et al. The low overpotential regime of acidic water oxidation part I: the importance of O₂ detection. *Energy Environ. Sci.* **15**, 1977–1987 (2022).
54. Righi, G. et al. On the origin of multihole oxygen evolution in haematite photoanodes. *Nat. Catal.* **5**, 888–899 (2022).

Publisher's note Springer Nature remains neutral with regard to jurisdictional claims in published maps and institutional affiliations.

Open Access This article is licensed under a Creative Commons Attribution 4.0 International License, which permits use, sharing, adaptation, distribution and reproduction in any medium or format, as long as you give appropriate credit to the original author(s) and the source, provide a link to the Creative Commons licence, and indicate if changes were made. The images or other third party material in this article are included in the article's Creative Commons licence, unless indicated otherwise in a credit line to the material. If material is not included in the article's Creative Commons licence and your intended use is not permitted by statutory regulation or exceeds the permitted use, you will need to obtain permission directly from the copyright holder. To view a copy of this licence, visit <http://creativecommons.org/licenses/by/4.0/>.

© The Author(s) 2026

¹Department of Materials, Imperial College London, London, UK. ²Department of Chemistry, Centre for Processable Electronics, Imperial College London (White City Campus), London, UK. ³Diamond Light Source, Harwell Science and Innovation Campus, Didcot, UK. ⁴Department of Chemistry, University of Copenhagen, Copenhagen, Denmark. ⁵Department of Materials, University of Manchester, Manchester, UK. ⁶Department of Chemistry, Chemistry Research Laboratory, Oxford University, Oxford, UK. ⁷Present address: Division of Chemistry and Chemical Engineering, California Institute of Technology, Pasadena, CA, USA. ✉e-mail: c.liang20@imperial.ac.uk; i.stephens@imperial.ac.uk; j.durrant@imperial.ac.uk; reshma.rao@imperial.ac.uk

Methods

DFT calculations

Spin-polarized DFT calculations were performed using the Vienna *ab initio* simulation package^{55,56} and the projector augmented-wave method^{57,58}. We used the Perdew–Burke–Ernzerhof exchange–correlation functional⁵⁹ for all the calculations with and without the inclusion of Hubbard *U* correction using the rotationally invariant DFT + *U* formalism⁶⁰ with *U* = 2.0 eV (ref. 61) for the *d* states of Ir atoms. The (110) surface of an IrO₂ rutile structure was modelled with a symmetric 3 × 1 slab with at least 30 Å of vacuum and six atomic layers, of which the two central layers were fixed in the optimized bulk geometry. Adsorbates were symmetrically placed on both sides of the slab at the Ir_{Cus} and Ir_{Bri} sites. The calculations were performed with a plane-wave energy of 500 eV and a 3 × 4 × 1 *k*-point mesh for the Brillouin zone integration. The convergence criteria were set to 10⁻⁴ eV for the electronic self-consistent iteration and 0.025 eV Å⁻¹ for the atomic forces on all atoms during ionic relaxations. The computational hydrogen electrode was used to consider the effect of the applied potential¹⁷ and the free energy changes as a function of applied potential were defined as

$$\Delta G_{\text{ads}}(U) = E_{\text{ads}}^{\text{DFT}} + \text{ZPE} + \int \text{Cd}T - T\Delta S - neU, \quad (4)$$

where *n* is the number of electrons for the considered reaction, and the ZPE, $\int \text{Cd}T$ and *T*Δ*S* terms were obtained from vibrational frequencies calculated via DFT used within the thermochemistry module from the atomic simulation environment package using the harmonic limit⁶² (Supplementary Table 1).

Synthesis of IrO_x

The hydrous amorphous IrO_x is prepared using an electrodeposition method reported in our previous reports^{21,22}. A solution containing 0.2 mmol of IrCl₃ hydrate (Fluorochem) and 1 mmol of oxalic acid dehydrate (Sigma-Aldrich) in 30 ml of water was prepared. The pH was adjusted to 10 with 5 mmol of K₂CO₃ (Sigma-Aldrich, ≥99.0%). The volume of the solution was then increased to 50 ml by adding another 20 ml of water. The solution was left to rest for 4 days at 35 °C and then stored in the refrigerator at 4 °C. The electrodeposition of IrO_x was conducted in a typical three-electrode setup in this solution. A Pt foil and an Ag/AgCl electrode are used as the counter and reference electrodes, respectively. IrO_x is deposited onto conductive substrates by applying an anodic current density of 35 μA cm⁻² for ~1,000 s. Fluorine-doped tin oxide (FTO) glass was used as the substrate for operando optical spectroscopy and Ir L-edge XAS measurements. Au-coated Si₃N₄ membranes were used for operando O K-edge XAS measurements, whereas glassy carbon was used as the substrate for EC-MS experiments.

Operando optical absorption spectroscopy

Operando optical absorption spectroscopy was performed on ~1 cm × 1 cm IrO_x samples on FTO substrates using a custom-built three-electrode setup, with a Pt counter electrode and a custom-built RHE. A 10-mW tungsten–halogen light source (Thorlabs SLS201L with an SLS201C collimator) illuminated the sample, and the transmitted light was collected via a 1-cm diameter liquid light guide (Edmund Optics) and directed to a spectrometer (Andor Kymera 193i) with a charge-coupled device camera (Andor iDus Du420A-BEX2-DD), cooled to -80 °C for an improved signal-to-noise ratio. Light was collimated and refocused using two 5-cm planoconvex lenses (Edmund Optics). An Autolab potentiostat controlled the potential in the potentiostatic mode, with 10-s equilibration at each step. Optical spectra were collected by averaging 30 acquisitions (~30 ms each), and current was recorded simultaneously using custom-built LabVIEW software version 2023 Q1 (National Instruments).

Operando NEXAFS

NEXAFS measurements were performed at the B07 beamline (B branch) at Diamond Light Source. Operando measurements were conducted using an in situ electrochemical cell described previously⁶³, incorporating a 100-nm-thick Si₃N₄ membrane window coated with 10-nm Ti and 10-nm Au (Silson). IrO_x was electrodeposited directly onto the Au layer. The membrane was sealed with an O-ring, and electrical contact was made via Au pins, with Pt wire and Ag/AgCl electrodes used as the counter and reference electrodes, respectively. The Ag/AgCl reference was calibrated against RHE. A 0.1-MHClO₄ electrolyte was continuously flowed through the cell at -10 μl s⁻¹ using a syringe pump. The electrolyte flow tube and connections to the working, reference and counter electrodes are integrated through a specially designed lid (DN63 CF flange) of the chamber, enabling it to maintain a low-pressure environment. O K-edge spectra were calibrated using the water pre edge at 535 eV and normalized to the post-edge region (~540 eV for operando and ~570 eV for ex situ measurements).

Operando Ir L-edge XAS

Operando XAS measurements were performed using a custom-built in situ electrochemical XAS cell in our previous report²¹, enabling measurements on electrodeposited IrO_x films on FTO under identical conditions to operando optical experiments. The cell accommodates different substrate types and sizes and operates as a standard three-electrode configuration. XAS measurements were carried out at the B18 beamline at Diamond Light Source using a Si(111) monochromator. Reference samples (Ir powder, IrCl₃ and IrO₂) were measured in the transmission mode, whereas the operando measurements of amorphous IrO_x were measured in the fluorescence mode. Energy calibration was performed using a Pt foil referenced to the Pt L₃ edge (11,564 eV). Before XAS, electrodes were conditioned by cyclic voltammetry between 0.6 and 1.45 V_{RHE} at 10 mV s⁻¹. The XAS spectra were collected during potential holds between -0.4 and -1.50 V_{RHE}, with ten spectra acquired and averaged at each potential. Data processing was performed using Athena version 0.9.26 (ref. 64). Time-resolved measurements were obtained by fixing the X-ray energy and monitoring the fluorescence intensity at 100-ms resolution, synchronized with the electrochemical data via system time stamps and normalized to the incident-beam intensity to exclude the background-intensity-fluctuating effect.

Chip-based EC-MS measurements

In situ gas analysis during electrochemical measurements was performed using a real-time on-chip EC-MS system (Spectro Inlets). The system is based on a microporous membrane chip fabricated from semiconductor-on-insulator wafers, consisting of an array of ~2.5-μm pores distributed over a 7-mm-diameter area. The electrolyte layer thickness was limited to ~100 μm to enable the rapid transfer of dissolved gases into the sampling volume for detection. IrO_x catalysts were electrodeposited on glassy carbon substrates and measured in a cell geometry analogous to a rotating disk electrode configuration. Mass spectrometry and electrochemical data were synchronized and analysed using the open-source package IXDAT (<https://ixdat.readthedocs.io/en/latest/>). Quantification of gaseous products was achieved by calibration against oxygen evolution on an oxidized Pt-disc electrode, assuming ~100% Faradaic efficiency at high potentials.

Data availability

The data supporting the findings of this study are available in the Supplementary Information. The datasets and analysis scripts underlying the figures are available via Zenodo at <https://doi.org/10.5281/zenodo.18320343> (ref. 65). Source data are provided with this paper.

References

55. Kresse, G. & Furthmüller, J. Efficient iterative schemes for *ab initio* total-energy calculations using a plane-wave basis set. *Phys. Rev. B* **54**, 11169–11186 (1996).

56. Kresse, G. & Hafner, J. Ab initio molecular dynamics for open-shell transition metals. *Phys. Rev. B* **48**, 13115–13118 (1993).
57. Kresse, G. & Joubert, D. From ultrasoft pseudopotentials to the projector augmented-wave method. *Phys. Rev. B* **59**, 1758–1775 (1999).
58. Blöchl, P. E. Projector augmented-wave method. *Phys. Rev. B* **50**, 17953–17979 (1994).
59. Perdew, J. P., Burke, K. & Ernzerhof, M. Generalized gradient approximation made simple. *Phys. Rev. Lett.* **77**, 3865–3868 (1996).
60. Dudarev, S. L., Botton, G. A., Savrasov, S. Y., Humphreys, C. J. & Sutton, A. P. Electron-energy-loss spectra and the structural stability of nickel oxide: an LSDA+*U* study. *Phys. Rev. B* **57**, 1505–1509 (1998).
61. Ping, Y., Galli, G. & Goddard, W. A. III Electronic structure of IrO₂: the role of the metal *d* orbitals. *J. Phys. Chem. C* **119**, 11570–11577 (2015).
62. Hjorth Larsen, A. et al. The atomic simulation environment—a Python library for working with atoms. *J. Phys. Condens. Matter* **29**, 273002 (2017).
63. Kumar, S. et al. An electrochemical flow cell for operando XPS and NEXAFS investigation of solid–liquid interfaces. *J. Phys.: Energy* **6**, 036001 (2024).
64. Ravel, B. & Newville, M. ATHENA, ARTEMIS, HEPHAESTUS: data analysis for X-ray absorption spectroscopy using IFEFFIT. *J. Synchrotron Radiat.* **12**, 537–541 (2005).
65. Liang, C. et al. Data for article ‘Key role of oxidising species driving water oxidation revealed by time resolved optical and X-ray spectroscopies’. *Zenodo* <https://doi.org/10.5281/zenodo.18320343> (2026).

Acknowledgements

C.L., I.E.L.S., J.R.D., R.R.R., S.J.H and M.A.T. would like to acknowledge funding and technical support from BP through the BP International Centre for Advanced Materials (bp-ICAM). C.L. also acknowledges Imperial College London and China Scholarship Council for the IC-CSC joint scholarship. We acknowledge Diamond Light Source for time on beamline B07 under proposal number SI34803 and beamline B18 under proposal numbers SP30396 and SP31886. This project was supported by the Royal Academy of Engineering under the Research Fellowship program (R.R.R.). This work was also supported by the Engineering and Physical Sciences Research Council (EP/W033232/1). Y.W. acknowledges support from EPSRC and SFI Centre for Doctoral Training in Advanced Characterisation of Materials

(grant reference number EP/SO23259/1). S.K. and G.H. thank Horizon 2020 grant 101017928 (HYSOLCHEM project) and the UKRI for International Science Partnerships Fund under award number ISPF-229, for funding. Via our membership of the UK’s HEC Materials Chemistry Consortium, which is funded by EPSRC (EP/X035859/1), this work used the ARCHER2 UK National Supercomputing Service (<http://www.archer2.ac.uk>). Transmission electron microscopy access was supported by the Henry Royce Institute for Advanced Materials, funded through EPSRC grants EP/RO0661X/1, EP/S019367/1, EP/P025021/1 and EP/P025498/1.

Author contributions

C.L. and R.R.R. conceived the ideas. C.L. carried out and analysed all experiments, unless otherwise stated. L.G.V. performed and analysed the theoretical calculations under the supervision of A.W. B.M. supported the optical and XAS measurements. S.B.S. assisted with the EC-MS measurements and data analysis. M.A.T. performed the transmission electron microscopy measurements and analysed the data under the supervision of S.J.H. S.K. designed the in situ cell of O K-edge X-ray absorption. P.F., D.C.G., S.K., Y.T., S.H., Y.W., C.T., R.R.R. and G.H. supported the O K-edge measurements and data analysis. V.C., B.M. and R.R.R. supported the Ir L-edge measurements and analysis. G.Y. performed the inductively coupled plasma mass spectrometry measurements. I.E.L.S., J.R.D. and R.R.R. supervised the project. C.L. wrote the manuscript with input from L.G.V., A.W., I.E.L.S., J.R.D. and R.R.R. All authors reviewed and edited the manuscript.

Competing interests

The authors declare no competing interests.

Additional information

Supplementary information The online version contains supplementary material available at <https://doi.org/10.1038/s41563-026-02514-9>.

Correspondence and requests for materials should be addressed to Caiwu Liang, Ifan E. L. Stephens, James R. Durrant or Reshma R. Rao.

Peer review information *Nature Materials* thanks Serhiy Cherevko, Pengtao Xu and the other, anonymous, reviewer(s) for their contribution to the peer review of this work.

Reprints and permissions information is available at www.nature.com/reprints.